International Journal of Refractory Metals and Hard Materials 95 (2021) 105439

Contents lists available at ScienceDirect

International Journal of Refractory Metals and Hard Materials

journal homepage: www.elsevier.com/locate/IJRMHM

Secondary phases effects on microstructure and mechanical properties of lanthanum-doped titanium-zirconium-molybdenum alloy

Bo-liang Hu [a,b], Kuai-she Wang [a,b,*], Ping Hu [a,b,*], Hai-rui Xing [a,b], Shi-Lei Li [a,b], Song-wei Ge [a,b], Jia-yu Han [a,b], Xing-jiang Hua [a,b], Jing-bo Fu [c], Alex A. Volinsky [d]

[a] School of Metallurgy Engineering, Xi'an University of Architecture and Technology, Xi'an 710055, China
[b] National and Local Joint Engineering Research Functional Center for Materials Processing, Xi'an University of Architecture and Technology, Xi'an 710055, China
[c] Jinduicheng Molybdenum Co., Ltd, Xi'an 710077, China
[d] Department of Mechanical Engineering, University of South Florida, Tampa, FL 33620, USA

ARTICLE INFO

Keywords:
La-TZM alloy
Secondary phases
Regulation
Microstructure
Mechanical properties

ABSTRACT

The size of the secondary phases affects the lanthanum-doped titanium-zirconium-molybdenum (La-TZM) alloy properties. In this study, the microstructure and mechanical properties of the La-TZM alloys were regulated by adding carbon and Ti/Zr elements, which resulted in different secondary phase characteristics. Adding nano-TiC and ZrC decreased the micron secondary phase size of the La-TZM alloy by 26.7%, and increased the yield strength by 27%, reaching 1239 MPa. The effects of secondary phase size and distribution on yield strength were analyzed. This study contributes to the design and theoretical analysis of new molybdenum alloys.

1. Introduction

Lanthanum-doped titanium-zirconium-molybdenum (La-TZM) alloy has better mechanical properties, higher recrystallization temperature and oxidation resistance, and lower ductile-to-brittle transition temperature than titanium-zirconium-molybdenum (TZM) alloy and other Mo alloys. Fine-grain strengthening, solid solution strengthening, and dispersion strengthening are effective methods to improve the mechanical properties of the La-TZM alloys [1].

Formation mechanisms of TiO_2, ZrO_2, ZrC, TiC, MoC, $ZrTiO_4$, La_2O_3, and $La_2Ti_2O_7$ secondary phases were analyzed for the La-TZM alloy [2]. Cracks are associated with the micron $La_2Ti_2O_7$ secondary phase. Thus, it is pivotal to reduce the quantity and size of the $La_2Ti_2O_7$ secondary phase in order to improve the alloy mechanical properties. The $La_2Ti_2O_7$ secondary phase is formed when La_2O_3, TiO_2, and ZrO_2 react at high temperatures. The original size of TiH_2 and ZrH_2 powders used for alloy preparation is 3–5 μm. In the process of alloy preparation, the size of added alloy powder is reduced by ball milling. Therefore, the size of the coarse $La_2Ti_2O_7$ secondary phase can be effectively reduced by lessening the formation of oxides or the size of original powder particles [3].

Browning et al. [4] took advantage of the nano-titanium carbide to improve TZM sintered density from 98.5% to 99% along with increasing alloy hardness by 75% and improving its flexural strength. Luo et al. [5] utilized carbon nanotubes (CNTs) to prepare Mo–0.5Ti–0.1Zr–0.03CNTs (wt%). The microstructure changes of the composite powders induced by ball milling improved the relative density, Vickers hardness, and yield strength. Goller et al. [6] added 5 wt% B_4C to the TZM alloy, which increased the hardness from 1.9 GPa to 7.8 GPa. Ahmadi et al. [7] added TiC and ZrC to TZM and produced TZM-20vol%TiC and TZM-20vol%ZrC (9.34 g/cm^3 density) samples. Grain size decreased to 6.5 μm for the TZM-20vol%TiC and 6.6 μm for the TZM-20vol%ZrC composites. The highest values of Vickers hardness were measured as 4.1 GPa for TZM-20vol%TiC and 3.88 GPa for TZM-20vol%ZrC. In summary, the mechanical properties of the TZM alloy can be improved by doping with TiC, CNTs, B_4C or ZrC. However, the above studies focused on the effects of alloying elements on the grain size, without an in-depth analysis of the alloying elements effects on mechanical properties.

In this paper, carbon, $Ti(SO_4)_2$, $Zr(NO_3)_4$, and nano TiC, ZrC were used to regulate the secondary phases in La-TZM alloys. The effects of carbon doping modes and Ti, Zr elements on the size and volume fraction of secondary phases and their corresponding effects on mechanical properties were studied. The improved strength and toughness of La-TZM alloy makes it one of the candidate materials for the replacement of zircon cladding tube in the core fuel of reactor in the future, and also makes it promising to be applied to the heat-resistant components of rocket and aircraft engines in the future.

* Corresponding authors.
E-mail addresses: wangkuaishe888@126.com (K.-s. Wang), huping1985@126.com (P. Hu).

https://doi.org/10.1016/j.ijrmhm.2020.105439
Received 14 September 2020; Received in revised form 10 November 2020; Accepted 10 November 2020
Available online 13 November 2020

2. Experimental procedures

With the same composition (Mo-0.5Ti-0.08Zr-1.0La-0.04C, wt%) and different alloying modes, different reducing agents were used for doping the alloy, including CNTs, fructose, and graphite as carbon sources, and TiH_2, ZrH_2, producing Mo-0.5TiH_2-0.08ZrH_2-3.0La$(NO_3)_3$–0.04CNT and Mo-0.5TiH_2-0.08ZrH_2–3.0La$(NO_3)_3$–0.12-Fructose, along with Mo-0.5TiH_2-0.08ZrH_2-3.0La$(NO_3)_3$–0.04Graphite and different Ti, Zr-doped producing Mo-3.0Ti$(SO_4)_2$–0.45Zr$(NO_3)_4$–3.0La$(NO_3)_3$–0.12Fructose and Mo-0.63TiC-0.11ZrC-3.0La$(NO_3)_3$–0.12Fructose (wt%) alloys.

The La-TZM alloys were produced via the powder metallurgy route using a mixture of Mo powder, Ti, Zr, C, and La elements. After these mixed powders were milled, they were cold isostatic pressed, sintered at 1950 °C and rolled into a 0.5 mm thick plate (95% deformation). The sintered billet sheet was used for the follow-up performance testing and observations.

An electronic universal tensile testing machine (Instron 8001, USA) was used for the tensile strength and yield strength measurements, and two samples were tested for each composition per ASTM E8. The microstructure of secondary phases was characterized by scanning electron microscope (SEM) equipped with energy-dispersive X-ray spectroscopy (EDS, Oxford 7718). For SEM investigations, samples from the as-sintered material were ground and polished. The hardness was tested by the digital Vickers micro-hardness tester (401 MVD). The microstructure of polished and $K_3[Fe(CN)_6]$:NaOH:H_2O = 10:1:1 etched samples were examined using SEM. The detailed microstructure of the precipitates was examined using transmission electron microscopy (TEM). Thin foil specimens were mechanically polished to ~30 μm thickness followed by double spray electrolytic milling for electron transparency.

3. Results and discussion

3.1. Secondary phases size and distribution

The La-TZM alloy microstructure is shown in Fig. 1. The grain sizes of Mo-0.5TiH_2-0.08ZrH_2-3.0La$(NO_3)_3$–0.04CNT, Mo-0.5TiH_2-0.08ZrH_2-3.0La$(NO_3)_3$–0.12Fructose, Mo-0.5TiH_2-0.08ZrH_2-3.0La$(NO_3)_3$–0.04-Graphite, Mo-3.0Ti$(SO_4)_2$–0.45Zr$(NO_3)_4$–3.0La$(NO_3)_3$–0.12Fructose and Mo-0.63TiC-0.11ZrC-3.0La$(NO_3)_3$–0.12Fructose are 17.86 ± 2 μm, 17.0 ± 1.76 μm, 15.85 ± 2 μm, 12.05 ± 1.6 μm and 32.89 ± 5.4 μm), respectively in Fig. 1(a), (d), (g), (j), and (m). Grain size slightly decreased from carbon nanotubes to graphite-doped La-TZM alloy. The grain size of Mo-Fructose-Ti$(SO_4)_2$-Zr$(NO_3)_4$-La$(NO_3)_3$ alloy is smaller than any other alloy, but the grain size of nano TiC-ZrC-doped alloy is the largest of all the alloys. In addition, spherical micrometer size secondary phase particles distribute around grains in Fig. 1(b), (e), (h), (k), and (n). These secondary phase particles are on the grain boundaries and hinder grain boundaries movement and grain growth.

With different alloying methods, the particle size of the secondary phases of La-TZM alloy was statistically analyzed, as shown in Fig. 1(c), (f), (i), (l), and (o). The average sizes of the micron secondary phase particles doped with CNT, fructose, graphite, Ti$(SO_4)_2$-Zr$(NO_3)_4$, and nano TiC-nano ZrC are 2.5 μm, 2.2 μm, 2.4 μm, 2.1 μm, and 1.8 μm, respectively. Among them, the particle sizes of different carbon-doped micron secondary phases are distributed in the 0–8 μm range, and the main size is distributed in the 1–3 μm range. The particle sizes of different Ti, Zr-doped micro secondary phases are distributed in the 0–4 μm range, and the main size is distributed in the 0–2 μm range. The secondary phase particles obtained by doping nano-TiC and nano-ZrC have the smallest particle size. In addition, the volume fraction of the micron secondary phase particles of different carbon sources are 6.16%, 6.02% and 6.05%, and Ti$(SO_4)_2$-Zr$(NO_3)_4$/TiC-ZrC doped alloy is 12.16% and 11.92%, respectively.

With the change of particle sizes and distribution, the grain size also changes. Through different alloying methods, one can effectively improve the microstructure, including grain size and distribution of the secondary phases. Alloying additives generate uniform fine secondary phase particles. Small secondary phases can effectively reduce fracture cracks in the coarse secondary phases.

3.2. Grain size control

La-TZM alloy prepared with different doping methods has different volume fraction and particle size of the secondary phases, and consequently, the grain size makes a difference. According to the theoretical calculation of grain size with secondary phase size and volume fraction (eq. 1), the calculated grain size of Mo-0.5TiH_2-0.08ZrH_2-3.0La$(NO_3)_3$–0.04CNT, Mo-0.5TiH_2-0.08ZrH_2-3.0La$(NO_3)_3$–0.12Fructose, Mo-0.5TiH_2-0.08ZrH_2-3.0La$(NO_3)_3$–0.04Graphite, Mo-3.0Ti$(SO_4)_2$–0.45Zr$(NO_3)_4$–3.0La$(NO_3)_3$–0.12Fructose and Mo-0.63TiC-0.11ZrC-3.0La$(NO_3)_3$–0.12Fructose are 40.1 μm, 36.4 μm, 39.2 μm, 17.5 μm and 15.2 μm, respectively.

$$d_f = \frac{d}{f} \tag{1}$$

Here, d_f is the new grain size, d is the average size of secondary phases particle, and f is the volume fraction of the secondary phases.

According to the Gladman's theory [13], the secondary phases control the grain size of the matrix. The criterion for the grain size of the secondary phases to be evenly distributed on spherical grains is as follows:

$$d_c = \frac{\pi d}{6f}\left(\frac{3}{2} - \frac{2}{Z}\right) \tag{2}$$

Here, d_c is the calculated grain size. Z=D_M/D_0 is the grain size inhomogeneity factor, where D_M is the largest grain, and D_0 is the average grain size. Uniformly pinned or weakly pinned solution after grain growth is when the Z value is up to 3, and the corresponding proportion coefficient Z is about 0.44. Uniform nail-pierced or strong abnormal grain growth in the aftermath of the pinned pierced solution is when the Z value is above 9, and the corresponding proportion coefficient is 0.67.

Fig. 2 is the theoretical calculation of the different pinning modes of the secondary phases. The secondary phases can produce pinning at the grain boundaries without coarsening at high temperatures, and the grain size of the five doped modes is different. The calculation results show that the grain size difference between homogenization pinning and non-homogenization pinning is about 9 μm, while the actual grain size is close to the homogenization pinning. Therefore, the secondary phases exist in homogenized Mo-0.5TiH_2-0.08ZrH_2-3.0La$(NO_3)_3$–0.04CNT, Mo-0.5TiH_2-0.08ZrH_2-3.0La$(NO_3)_3$–0.12Fructose, Mo-0.5TiH_2-0.08ZrH_2–3.0La$(NO_3)_3$–0.04Graphite, Mo-3.0Ti$(SO_4)_2$–0.45Zr$(NO_3)_4$–3.0La$(NO_3)_3$–0.12Fructose alloy has non-homogenization pinning, and Mo-0.63TiC-0.11ZrC-3.0La$(NO_3)_3$–0.12Fructose alloy has neither homogenization pinning, nor non-homogenization pinning.

The secondary phase particles size of the Mo-0.63TiC-0.11ZrC-3.0La$(NO_3)_3$–0.12Fructose alloy decreased, but the main grain size increased by 93.5%. Gladman and Rohrer considered that the smaller secondary phase particles can pronounce dragging of a moving grain boundary [13–14]. Eq. (3) represents the pinning force of the secondary phase for the grain boundary:

$$f_{\max} = 1.5c\gamma/r \tag{3}$$

Here, r is the spherical particle radius, γ is the specific energy of planar grain boundary, c is the volume fraction of the particles, which is equal to $4/3\pi r^3 N$, and N is the number of particles.

Recrystallization and grain growth are described by the Zener eq. (2) for the two-phase alloys. The coherent interface makes the boundary sweep the particle according to Gottstein & Shvindlerman [15]. Thus, the reason for the increase in grain size is because the volume fraction of

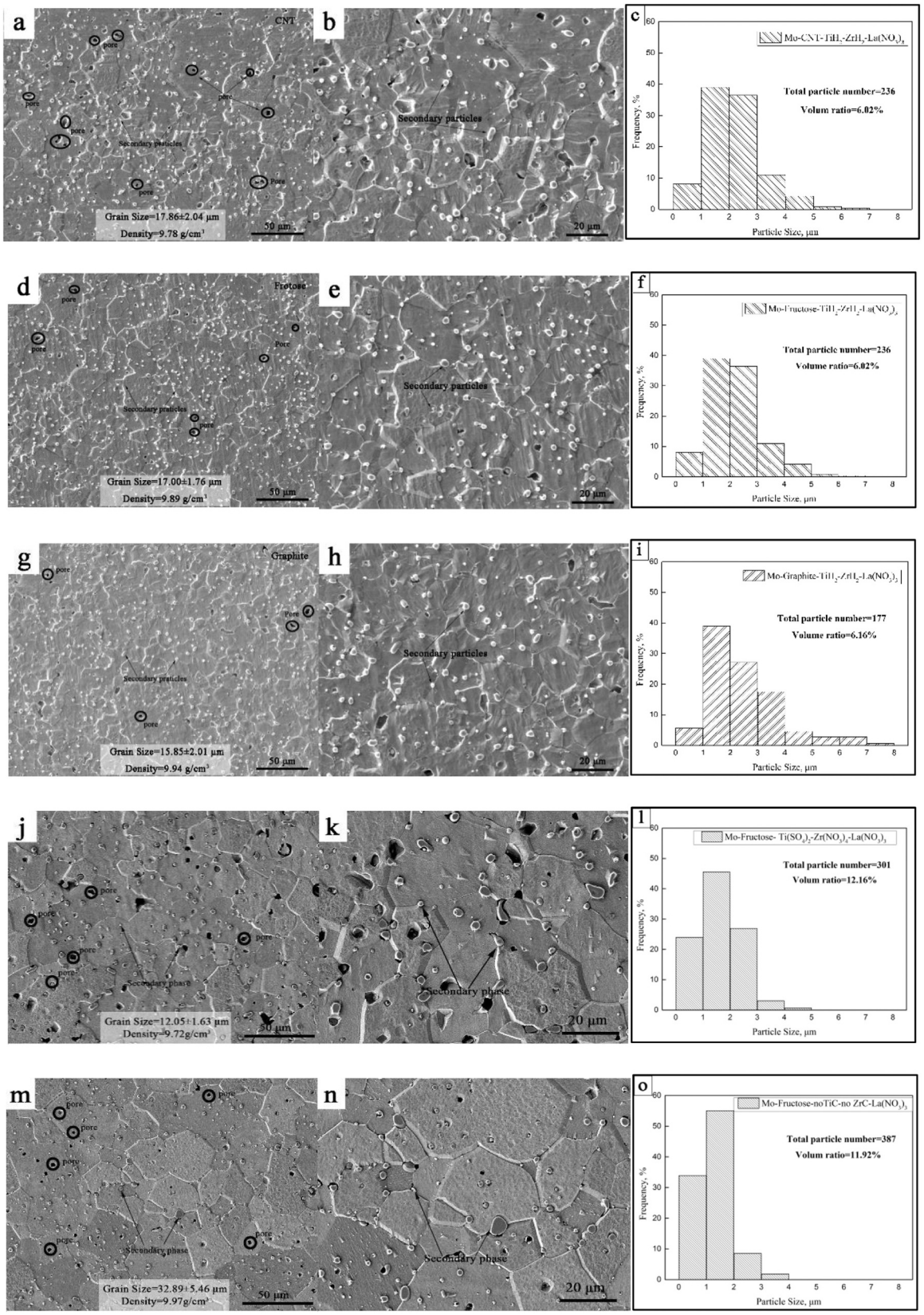

Fig. 1. The microstructure of the La-TZM alloy with different alloying elements: (a, b) Mo-0.5TiH_2-0.08ZrH_2-3.0$La(NO_3)_3$–0.04CNT; (c) statistical data analysis of secondary phase particles in (b); (d, e) Mo-0.5TiH_2-0.08ZrH_2-3.0$La(NO_3)_3$–0.12Fructose; (f) statistical data analysis of secondary phase particles in (e); (g, h) Mo-0.5TiH_2-0.08ZrH_2-3.0$La(NO_3)_3$–0.04Graphite; (i) statistical data analysis of secondary phase particles in (h); (j, k) Mo-3.0$Ti(SO_4)_2$–0.45$Zr(NO_3)_4$–3.0La$(NO_3)_3$–0.12Fructose; (l) the statistical data analysis of secondary phase particles in (k); (m, n) Mo-0.63TiC-0.11ZrC-3.0$La(NO_3)_3$–0.12Fructose; (o) the statistical data analysis of secondary phase particles in (n).

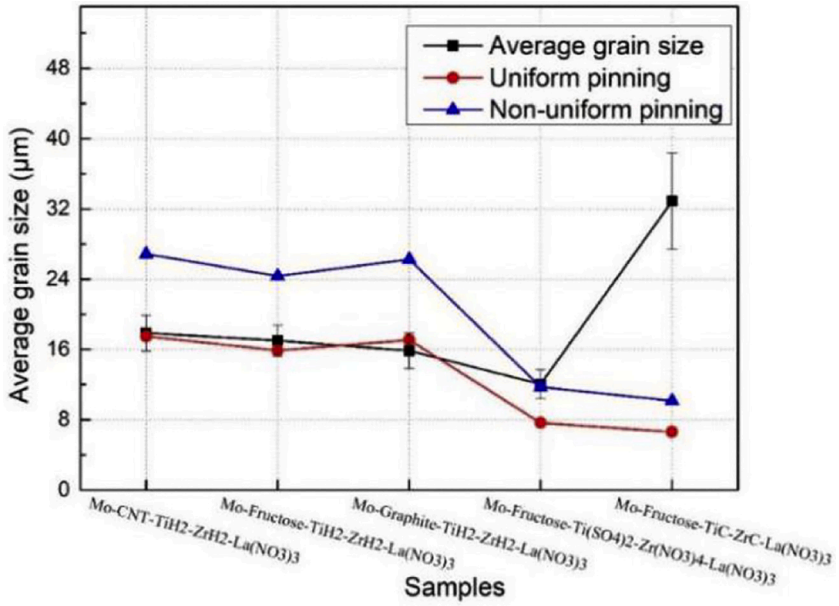

Fig. 2. Calculation of the secondary phases grain size for different pinning methods.

the micron secondary phases at the grain boundary reaches 11.9%, and the micron secondary phase particles get distributed at the grain boundary, while the nano-secondary phase particles are mainly distributed inside the grains. The microstructure is strip-like in Fig. 3(a). There are fewer nanometer secondary phase particles in Fig. 3(b) and (c). The size of the micrometer secondary phase is 1.8 μm in Fig. 3(d). The nanometer secondary phase in the crystal and the micron size secondary phase at the grain boundary cannot prevent the growth of grains.

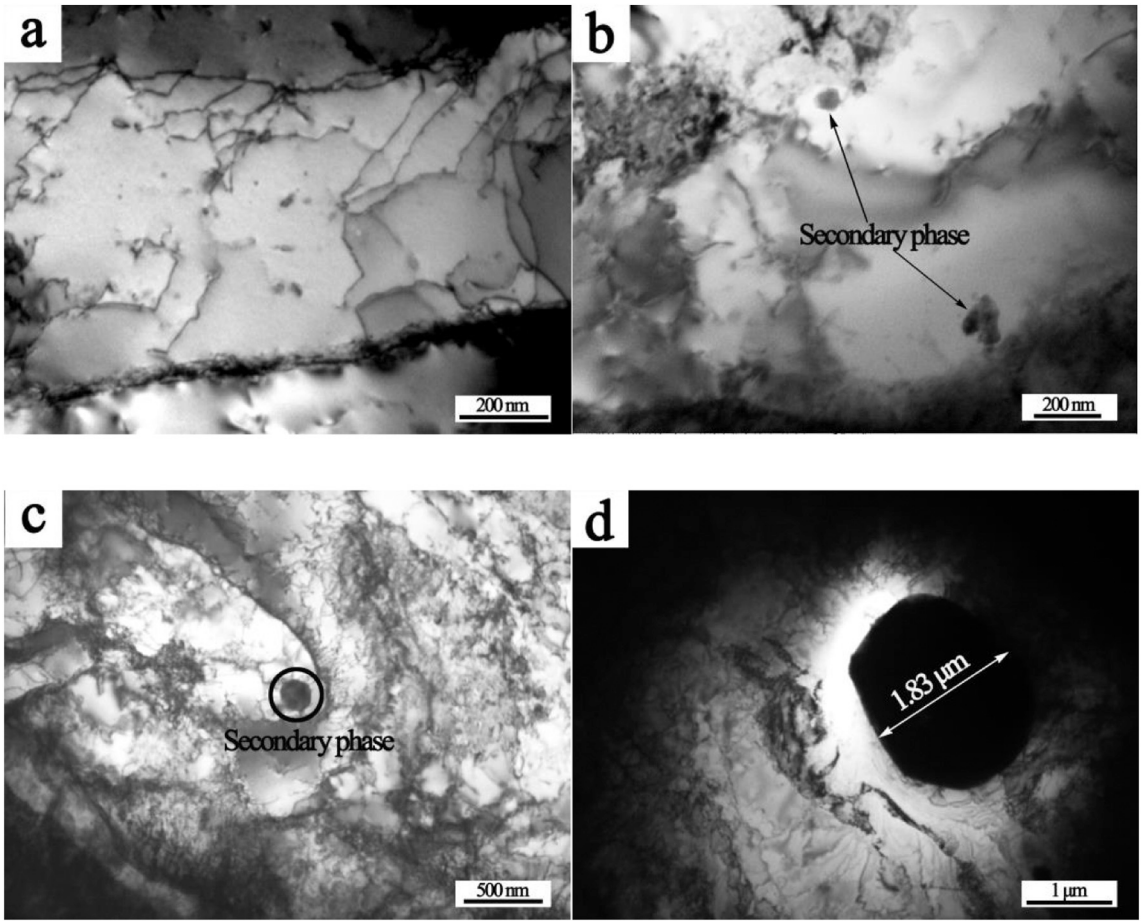

Fig. 3. TEM microstructure of the Mo-Fructose-TiC-ZrC-La(NO_3)$_3$ alloy (a, strip-like microstructure; b&c intragranular nano secondary phase; d, intragranular micron secondary phase.)

Thus, the grain size of Mo-0.63TiC-0.11ZrC-3.0La$(NO_3)_3$–0.12Fructose alloy reaches 33 ± 5.4 μm. The large uniform grain size reduces the mechanical properties of the alloy but increases its high-temperature stability.

3.3. Different alloying modes properties

The hardness and yield strength values of the La-TZM alloy sintered blank and rolled plate with different alloying methods are shown in Fig. 4: Mo-0.5TiH_2-0.08ZrH_2-3.0La$(NO_3)_3$–0.04CNT alloy (175 ± 15 HV, 1018 ± 23 MPa), Mo-0.5TiH_2-0.08ZrH_2-3.0La$(NO_3)_3$–0.12Fructose alloy (189 ± 7 HV, 1060 ± 22 MPa), Mo-0.5TiH_2-0.08ZrH_2-3.0La$(NO_3)_3$–0.04Graphite alloy (205 ± 12 HV, 1055 ± 5 MPa), Mo-3.0Ti$(SO_4)_2$–0.45Zr$(NO_3)_4$–3.0La$(NO_3)_3$–0.12Fructose alloy (162 ± 2 HV, 1104 ± 3 MPa), Mo-0.63TiC-0.11ZrC-3.0La$(NO_3)_3$–0.12Fructose alloy (146 ± 1 HV, 1293 ± 14 MPa. The yield strength, tensile strength, and elongation of the Mo-0.63TiC-0.11ZrC-3.0La$(NO_3)_3$–0.12Fructose plate are 1025 ± 21 MPa, 1253 ± 33 MPa, and 9.5% after annealing at 950 °C for 1 h. It can be seen that the Mo-0.5TiH_2-0.08ZrH_2-3.0La$(NO_3)_3$–0.04Graphite sintering billet has the highest hardness. After rolling, the yield strength reaches 1293 ± 14 MPa. Compared with the Mo-0.5TiH_2-0.08ZrH_2-3.0La$(NO_3)_3$–0.04Graphite alloy, the yield strength increased by 27%. The tensile strength of the annealed alloy decreased by 22%, but the elongation increased from 2% to 9.5%. Refined secondary phase particles effectively increased the yield and tensile strength by hindering dislocations.

3.4. Micron secondary phases enhancement

According to the multi-scale microstructure of the La-TZM alloy, the fine grain structure and micron size distribution of different alloying methods were observed at the grain boundaries and inside the grains. The secondary phases of the La-TZM alloy are mainly composed of TiO_2, ZrO_2, TiC, ZrC, La_2O_3, MoC, $ZrTiO_4$, and $La_2Ti_2O_7$. These formed phases are high-strength ceramic phases, which belong to non-deformed particles. The non-deformable secondary phase reinforcement is represented by eq. (4).

$$\sigma_p = \frac{\Phi G b}{d_{particle}} \left(\frac{6 f_{particle} f_{Mo}}{\pi} \right)^{1/2} \tag{4}$$

Here, Φ represents the Taylor factor, G and b are the shear modulus and Burgers vector, f_{Mo}, and $f_{particle}$ are the volume fraction of the Mo phase and particles, and $d_{particle}$ is particle size. Muñoz-Morris et al. [8] have taken the Taylor factor as 2.5 for the bcc crystal structure. The shear modulus of molybdenum alloy is taken as 140 GPa and the Burgers vector in the (a/2 ⟨111⟩) crystal orientation is 2.72×10^{-10} m according to Zhang et al. [9]. Analyzing statistical results in Fig. 1, the values of micron secondary phase enhancement (σ_P) for the La-TZM alloys are obtained.

The micron phase particles strengthening effect by the Orowan strengthening of the Mo-0.5TiH_2-0.08ZrH_2-3.0La$(NO_3)_3$–0.04CNT, Mo-0.5TiH_2-0.08ZrH_2–3.0La$(NO_3)_3$–0.12Fructose, Mo-0.5TiH_2-0.08ZrH_2-3.0La$(NO_3)_3$–0.04Graphite, Mo-3.0Ti$(SO_4)_2$–0.45Zr$(NO_3)_4$–3.0La$(NO_3)_3$–0.12Fructose and Mo-0.63TiC-0.11ZrC- 3.0La$(NO_3)_3$–0.12-Fructose alloys increased their strength by 12.8 MPa, 14.3 MPa, 13.2 MPa, 20.1 MPa, and 23.5 MPa, respectively.

The effects of different carbon sources (CNT, fructose, graphite), Ti$(SO_4)_2$/Zr$(NO_3)_4$, and TiC, ZrC-doped La-TZM alloy were 1.26%, 1.35%, 1.25%, 1.82%, and 1.82%, respectively. This shows that the proportion of the secondary phases strengthening is different for different doping modes. The smaller the particle size of the micron secondary phases, the higher the strengthening effect. However, the micro-secondary phase particle strengthening effect of different C sources and Ti, Zr elements was not significant, since for the La-TZM alloy nanoparticles, phase precipitation strengthening plays a leading role in the improvement of yield strength. By comparison, the Mo-0.63TiC-0.11ZrC-3.0La$(NO_3)_3$–0.12Fructose alloy exhibits higher yield strength and the grain size is larger. The nanoparticle precipitation strengthening affects the strength differently.

In the sintered blank, the hardness value is related to the secondary phase particles, especially those with a micron size. The secondary phase type is the same in different doping modes, consequently, the larger the micron particle size is, the larger the hardness, which is consistent with the size of micron phase particles in the La-TZM alloy with different alloying elements. It can be seen from the test data that the hardness of the sintered blank is inversely proportional to the yield strength. The microstructure can be effectively regulated by alloying and reduction of alloying elements. The secondary phases refinement and the reduction of coarse particles have different effects on the hardness and yield strength. They reduce the hardness and effectively improve the yield strength. The initial amount of added elements is the same, and the increase of the size of coarse and large micron phase particles leads to the decrease of the strengthening. In plate processing, the strengthening effect of the nanometer phase is significantly higher than of the micron phase, and accordingly, the yield strength increases significantly with the decrease of the coarse and large micron phases.

As shown in Fig. 5, La-TZM alloy was prepared by sintering, hot, warm, and cold-rolling. The different scales of particle phases appeared in the matrix, and the microparticles and nanometer particle phases before the recrystallization temperature exist in the grain boundary in

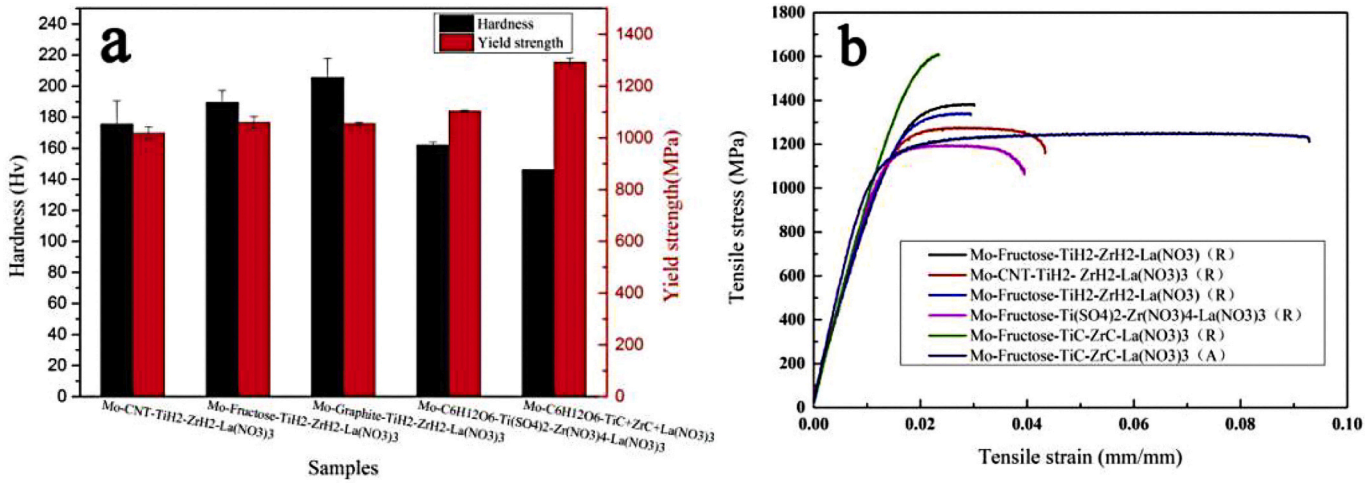

Fig. 4. Hardness and yield strength of the La-TZM alloy doped with different elements: (a) hardness and yield strength; (b) tensile stress-strain curves.

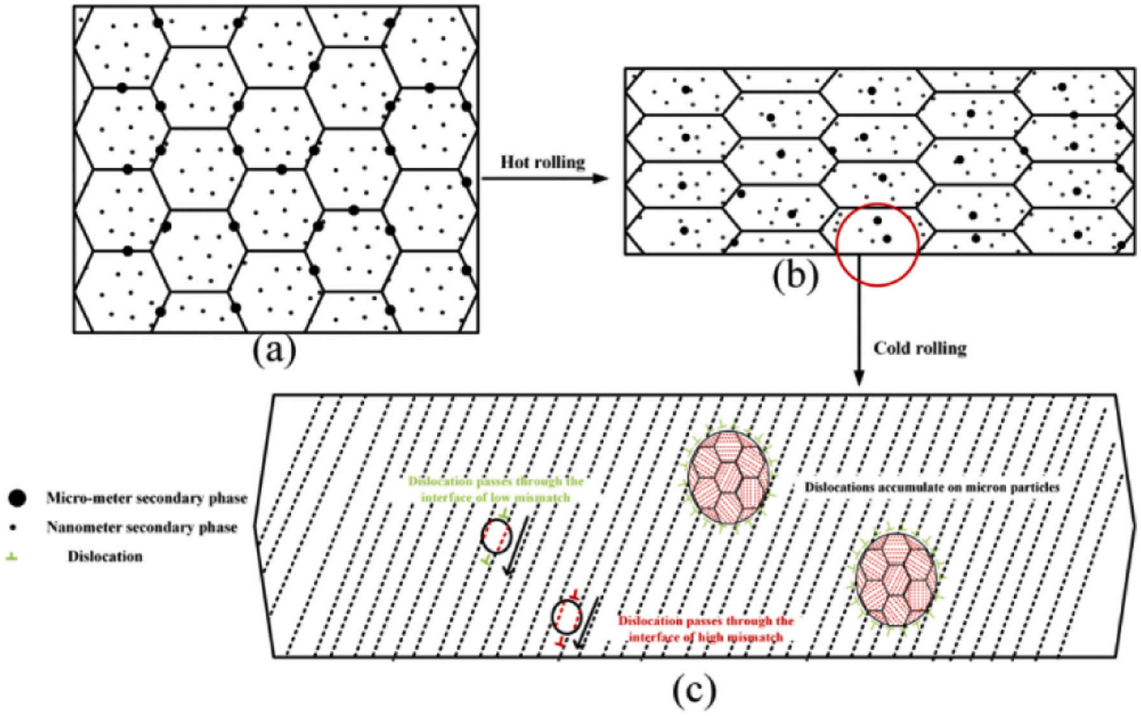

Fig. 5. Evolution and synergistic mechanisms of secondary phases in high-strength La-TZM alloy: (a) the secondary phase distribute in the sintered blank; (b) the secondary phase distribute in hot rolled tissue; (c) The secondary phase distribute in the cold-rolled tissue.

Fig. 5(a). Above the recrystallization temperature, the grain boundary migration and the majority of micro and nanoparticles are inside the grain in Fig. 5(b). The grains get crushed during tensile deformation and nano/micro secondary phases at the grain boundary during the hot rolling deformation processes. However, some secondary phases are still located inside the grains. Until cold rolling deformation, many dislocations and strengthening phase particles interact. The mismatch degree was achieved through different nanometer particles and micron particles. When dislocations meet the lower mismatch nanoparticles, dislocations glide through the particle phase under low stress. When the dislocations meet the higher mismatch particles, more stress was needed to pass. Therefore, the strengthening effect caused by nanoparticles, and the higher the degree of mismatch, the higher the reinforcement in Fig. 5(c). When a dislocation wants to pass through the micron particles, it doesn't pass because the particles are polycrystalline and arrange into complex grains. A large number of dislocations start to accumulate around the micron phase, so the stress concentration is receded at the grain boundary. The deformation of the microphase particles effectively reduces the distribution configuration of dislocations, thus improving toughness. However, the micron phase particles had a weak effect on the strength improvement of the material in Fig. 5(c).

The $La_2Ti_2O_7$ micro secondary phase has a low degree of mismatch with the matrix. The small size of the micron particle phase accumulates a small number of dislocations but does not lead to premature crack formation. This structure changed the dislocation configuration. The weak interface bond strength is more conducive to energy dissipation in the process of fracture, so a small amount of uniformly distributed $La_2Ti_2O_7$ micron particles help alloy plasticity. Nanometer particles, including TiC, La_2O_3, TiO_2, and others, produce reinforcement and coherent ZrC dislocations after reinforcement, reducing the quantity or size of the $La_2Ti_2O_7$ phase, which can significantly change the structure and improve the strength.

4. Conclusions

(1) The microstructure and properties of the La-TZM alloy can be regulated by different C sources, $Ti(SO_4)_2$, $Zr(NO_3)_4$ and nano TiC, ZrC particles.

(2) The size of the secondary phases of the nano-TiC/ZrC-doped La-TZM alloy is not uniform, and the main distribution of the nanometer phase and the internal crystals leads to the grain size in the sintering process of 33 ± 5 μm, larger than other alloys.

(3) The calculation of pinning type of secondary phase in La-TZM alloy shows that Mo-0.5TiH_2-0.08ZrH_2-3.0$La(NO_3)_3$–0.04CNT, Mo-0.5TiH_2-0.08ZrH_2-3.0$La(NO_3)_3$–0.12Fructose, and Mo-0.5TiH_2-0.08ZrH_2-3.0$La(NO_3)_3$–0.04Graphite alloys have homogenization pinning, Mo-3.0$Ti(SO_4)_2$–0.45$Zr(NO_3)_4$–3.0$La(NO_3)_3$–0.12Fructose alloy has non-homogenization pinning, Mo-0.63TiC-0.11ZrC-3.0$La(NO_3)_3$–0.12Fructose alloy has neither homogenization nor non-homogenization pinning.

(4) Among La-TZM molybdenum alloys doping methods, the highest strength was achieved by the Mo-0.63TiC-0.11ZrC-3.0$La(NO_3)_3$–0.12Fructose alloy (1293 ± 14 MPa), while the yield strength of the Mo-0.5TiH_2-0.08ZrH_2-3.0$La(NO_3)_3$–0.04CNT alloy was the lowest, among which the increase of the volume fraction of micron phase was the main reason for the decrease of yield strength.

Author statement

Under supervision by Prof. Kuai-she Wang & Ping Hu, Bo-liang HU, Jia-yu Han, and Song-wei Ge, Jing-bo Fu performed sample preparation and Characterization. Hai-rui Xing, Shi-lei Li and Xing-jiang Hua performed data analysis. Bo-liang HU, Kuai-she Wang and Ping HU developed mechanics modelling and analysis. Bo-liang HU and Alex A. Volinsky performed writing and language polishing. All authors read and contributed to the manuscript.

Declaration of Competing Interest

None.

Acknowledgments

This work was supported by the Major scientific and technological projects in Shaanxi Province of China [2020ZDZX04-02-01], the Fok Ying Tung Education Foundation [171101] and the Youth Innovation Team of Shaanxi Universities [2019-2022], and the Outstanding Doctoral Thesis Cultivation Fund of Xi'an University of Architecture and Technology [6040318007], the top young talents project of "Special Support Program for High Level Talents" in the Shaanxi Province (2018-2023).

References

[1] P. Hu, B.L. Hu, K.S. Wang, R. Song, F. Yang, Z.T. Yu, J.F. Tan, W.C. Cao, D.X. Liu, G. An, L. Guo, H.L. Yu, Strengthening and elongation mechanism of lanthanum-doped titanium-zirconium- molybdenum alloy, Mat. Sci. Eng. A-Struct. 678 (2016) 315–319, https://doi.org/10.1016/j.msea.2016. 10.013.

[2] B.L. Hu, K.S. Wang, P. Hu, Y.H. Zhou, J. Deng, W.J. Chen, P.F. Feng, J.P. Zhang, A. A. Volinsky, H.L. Yu, Secondary phases formation in lanthanum-doped titanium-zirconium-molybdenum alloy, J. Alloy. Compd. 757 (2018) 340–347, https://doi.org/10.1016/j.jallcom.2018.05.103.

[3] B.L. Hu, K.S. Wang, P. Hu, S.L. Li, J. Deng, Zuo Yg, Xing Hr, P.F. Feng, V. Paley, A. A. Volinsky, Fracture behavior of the La-doped molybdenum-titanium-zirconium alloy, Mater. Sci. Eng. A 759 (2019) 167–171, https://doi.org/10.1016/j.msea.2019.05.031.

[4] P.N. Browning, J. Fignar, A. Kulkarni, J. Singh, Sintering behavior and mechanical properties of Mo-TZM alloyed with nanotitanium carbide, Int. J. Refract. Met. H 62 (2017) 78–84, https://doi.org/10.1016/j.ijrmhm.2016.10.002.

[5] Y. Wei, L.M. Luo, X. Zan, J.P. Song, X.Y. Zhu, Y.C. Wu, Microstructural evolution and mechanical properties of carbon nanotubes–reinforced TZM composites synthesized by powder metallurgy, J. Alloy Compd. 829 (2020) 154540, https://doi.org/10.1016/j.jallcom.2020.154540.

[6] B. Yavas, G. Goller, Investigation the effect of B_4C addition on properties of TZM alloy prepared by spark plasma sintering, Int. J. Refract. Met. H 58 (2016) 182–188, https://doi.org/10.1016/j. ijrmhm.2016.04.020.

[7] E. Ahmadi, M. Malekzadeh, S.K. Sadrnezhaad, Preparation of nanostructured high-temperature TZM alloy by mechanical alloying and sintering, Int. J. Refract. met. H 29 (1) (2011) 141–145, https://doi.org/10.1016/j.ijrmhm.2010.09.003.

[8] M.A. Mun Oz-Morris, C.G. Oca, D.G. Morris, An analysis of strengthening mechanisms in a mechanically alloyed, oxide dispersion strengthened iron aluminide intermetallic, Acta Mater. 50 (11) (2002) 2825–2836, https://doi.org/10.1016/s1359-6454(02)00101-5.

[9] G.J. Zhang, Y.J. Sun, C. Zuo, J.F. Wei, J. Sun, Microstructure and mechanical properties of multi-components rare earth oxide-doped molybdenum alloys, Mat Sci. Eng. A-Struct. 483-484 (2008) 350–352, https://doi.org/10.1016/j.msea.2006.08.143.